Measuring Scattering Off the LIGO Hanford Observatory Test Masses

Christian Pluchar, Amherst College
Mentor: Keita Kawabe, LHO

September 22, 2017

Abstract

The Advanced LIGO detectors are interferometers that measure the change in distance between two test masses in order to detect gravitational waves from astronomical sources. The detector design utilizes Fabry-Perot optical cavities to increase the effective length of the arms and increases the power circulating in the cavities to over 100 kilowatts. Light scattering off of the test masses introduces a significant source of noise which is difficult to measure while the interferometer is locked. DSLR cameras have been installed at the LIGO Hanford Observatory and can be used to observe the wide angle scattering of the test masses. In order to measure the scattered power, the cameras were first calibrated to equate the CMOS sensor output to the corresponding incident energy. Images of the scattering were then captured for ETMx and ITMx, and the calibration was used to find the amount of power incident on the sensor. A number of techniques for improving the initial estimates, including subtracting the read noise of the camera, determining the quantum efficiency of the sensor, and extending the dynamic range are also discussed.

Contents

1 Introduction

The LIGO detectors are modified Michaelson Morley interferometers, with 4 kilometer long Fabry-Perot resonant cavities. The interferometer is sensitve to changes in length between test masses situated at the ends of each arm smaller than 10^{-20} meters. In order to increase the effective length of the interferometer, Fabry-Perot resonant optical cavities are formed in each arm between the end and input test masses. The cavities increase the power circulating in the detector to above 100 kilowatts, therefore increasing the power incident on the test mass surfaces. The test masses are made of fused silica glass and both the input test mass and end test masses have very low absorption rates, along with surface level imperfections on the order of nanometers in order to limit scattering [1]. Additional scattering can be caused by imperfect application of various surface coatings from manufacturing and installation of the test masses [2].

Reducing the intensity of scattering off the test masses will decrease noise in the detectors. As light is scattered out of the main beam, the reduction in laser power increases the relative amount of shot noise in the detector, as the displacement sensitivity limited by the shot noise is inversely proportional to the square root of the circulating power [3, p. 79]. Shot noise is one of the limiting sources of noise at high frequencies [3, p. 74]. Scattered light can also introduce noise if it recombines with the main beam. Because this light has traveled a different distance than the main beam, it will change the net phase of the main beam [3, p. 99].

While there have been efforts to characterize the optical performance of the test mass outside of the detector, it is desirable to have a system at the detectors which can measure the scattering off the test masses while the interferometer is observing. Previous methods to measure scattering include using photodiodes [4] and GigE cameras [2]. The method described here utilizes DSLR cameras to image and measure the power of the scattering off the test masses. DSLR cameras have many advantages over these systems, including large image sensors, which allows for better spatial resolution to identify different features of the scattering and the availability of many high performance lenses to zoom in on the test masses.

In this project, a calibration was performed for the DSLR cameras available to be used at the LIGO Hanford Observatory, the Nikon D7100 and Nikon D810. Images of the test mass scattering were then captured using DSLR cameras installed as part of the photon calibration (Pcal) system while the interferometer was locked. Using the measured camera calibration, an estimate for the wide angle scattering power of the x-arm input test mass (ITMx) and end test mass (ETMx) were calculated.

2 Methods

2.1 Camera Calibration

Camera sensors use photosensitive semiconductors to absorb photons of certain wavelengths, which results in the production of current. Additional electronics then amplify the current and convert the analog signal into a digital count which the camera then records. A typical

sensor has millions of these photosites, and the camera combines the signal from each to produce a matrix of digital numbers which corresponds to the amount of light absorbed by the sensor at each location in the sensor matrix. In the CMOS sensor of the Nikon D7100 and D810 cameras being used, each pixel site has its own amplifier, and the current is turned into a corresponding digital number based on the specifics of the camera and its settings [5]. The sensor is fitted with a color filter array known as a Bayer array (Figure 1) in order to create color images with a similar color palette as the human eye [6]. The filter is colored red, green, and blue, and allows those frequencies to pass to specific sections on the sensor.

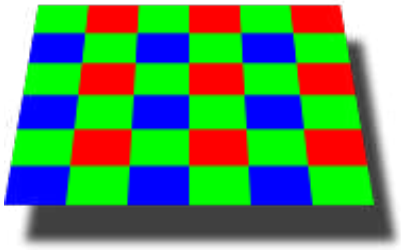

Figure 1: Illustration of a Bayer array [7].

The main lasers of the LIGO detectors have a wavelength of 1064 nanometers [8], which the camera sensor still is sensitive to, despite it being in the infrared range. In order to increase the response to this wavelength of light, the IR filter installed in the camera was removed by the manufacturer. Calibration was first performed with a 980 nanometer laser to refine the data collection and analysis process, and then with a 1064 nanometer laser to match the wavelength used in the detector.

The camera calibration converts the digital output of the camera sensor into a quantity of energy incident on the sensor for a particular wavelength of light. To perform the calibration, the camera was first placed on a tripod with the lens removed. The lens was removed because different lenses are being used across the detector, which each having a different transmissivity. A laser was placed on an adjacent optical table with the beam incident on the sensor (see Figure 2). The lights of the room were turned off, and exposures were taken using different shutter speeds and laser powers. The laser beam profile (size of the beam on the image sensor) was also varied between a "wide" and "narrow" projection. Previous results indicated the calibration may depend on the beam profile of the laser [9]. If the calibration were dependent on the beam profile, it would pose a significant challenge for accurately measuring the scattered power off the test masses, as the scattering has its own unique profile.

The power emitted by the laser was measured by a Ophir PD300 photodiode power sensor with the attenuating filter removed. Care was taken in order to ensure the entire beam was directed on the sensor and that a minimum numbers of pixels were overexposed (saturated). The camera has a maximum value for each pixel site in the sensor array, and when this saturation value is reached, the camera can no longer record additional pixel counts. A series of photos were also taken with the laser turned off in order to measure the ambient

light in the room. The ISO of the camera was kept constant at 200, and the image color depth was set to 14 bits.

A Python script using Rawpy [10] was then utilized to determine the pixel counts in each of the images across the red, green, and blue color channels from the RAW files produced. The number of pixel counts for each channel was then plotted against the incident laser energy, calculated by multiplying the measured power output of the laser by the exposure time of the camera.

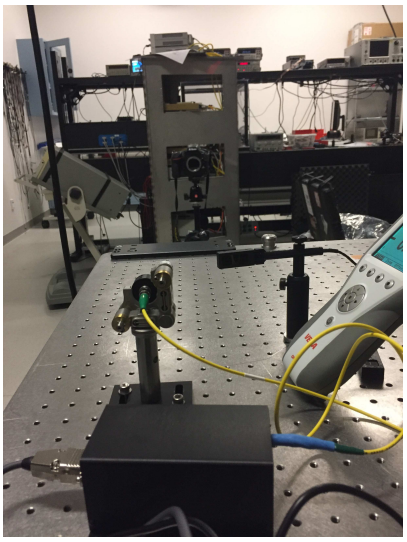

Figure 2: Experimental setup for camera calibration. In the foreground, the 1064nm laser and its power supply rests on an optical table, directed at a DSLR camera with the lens removed. The power meter used to measure the power output of the laser sits to the right.

2.2 Measuring Optical Scattering from LHO Test Masses

DSLR cameras have been previously installed at viewports across the detector (Figure 3). At the end stations, these have been added in order to observe the beam positioning of the photon calibrator on the test masses [11].

The cameras are controlled by remote capture software (Figure 4). The camera observing ETMx was used to capture images of the scattering. First, images were captured while the interferometer was out of lock and the main laser was turned off in order to get a measure of the ambient light from auxilliary lasers, such as the optical lever. Then, images were captured at a number of different exposure times while the interferometer was in lock with 30 watts of input power. The camera ISO was kept constant at 100, while the shutter speed was varied. Previously captured images of ITMx will be used as well in analysis, and a similar method was used to capture these images [12]. Using the calibration information of the camera and these images, an estimate for the wide angle scatter off the test masses can be made.

Figure 3: Pcal camera (black box) installed to observe test mass scattering at ETMx.

2.3 Camera Sensor Quantum Efficiency

An attempt was made to measure the quantum efficiency of the camera sensor. The quantum efficiency is a measure of how many photons incident on the sensor are absorbed by the sensor and result in the production of electrons. Measuring the quantum efficiency gives a better estimate of the uncertainty in the measurement of the energy incident on the camera. Typical CMOS sensors will have quantum efficiencies much less than one because some area of the sensor is covered by amplifiers and other electronics instead of photosentive components [5]. Quantum efficiency is also frequency dependent. The photosensors used in the camera sensor have a frequency dependent quantum efficiency, in addition to the frequency dependent transmissivity of the Bayer filter on top of it (the transmission of red and blue light through the green sections of glass is close to zero).

The noise in the power output of a laser is limited fundamentally by shot noise. Because photons are discrete units, the number emitted by the source varies slightly in time because the emission of a single photon is roughly a random process. Therefore, the distribution of the number of photons emitted can be described by Poisson statistics, so if the mean number of photons emitted is N, then the standard deviation in the number of photons emitted is $\sqrt{N}$. The camera will register some number of pixel counts,

$$N_{pix} = QN, \tag{1}$$

where Q is the quantum efficiency. By measuring the standard deviation in the number of pixel counts across exposures, the shot noise can be measured, along with the number of incident photons.

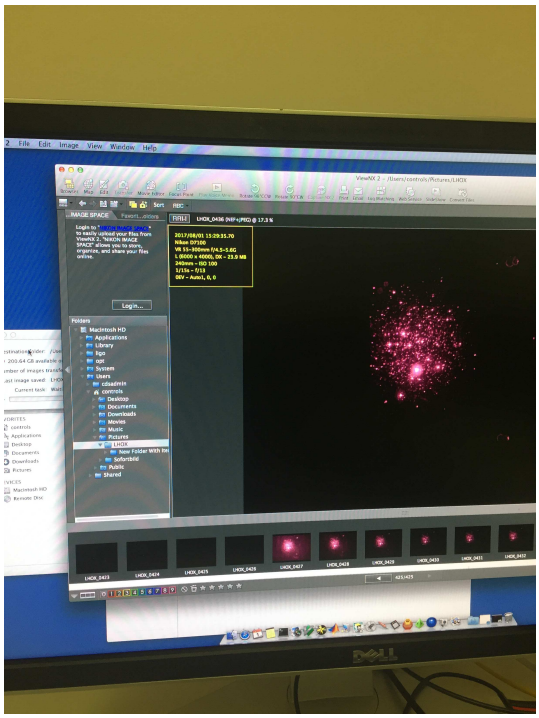

Figure 4: The remote camera software which was used to capture images of the ETMx scattering.

There are additional sources of noise which complicate this measurement. Typically, other sources of variation in the power output of the laser are well above the shot noise limit. Collectively, they will be referred to as intensity noise. Slow variation in the power output is one source of intensity noise. Relative intensity noise is defined as the intensity fluctuation normalized by the mean intensity of light. We assume the relative intensity noise is equal over the entirety of the laser beam. Therefore, the intensity noise (variation in the number of photons) will be proportional to the number of photons for some chosen time period. The constant of proportionality will be the same across all pixels. Read noise originates from the camera converting the charge at each photosite into a voltage as part of the analog to digital conversion. A simplifying assumption was made that the read noise at each photosite was identical, however because each pixel of a CMOS has its own analog to digital converter, and the read noise from each component will be slightly different [5].

Adding these sources of noise together, the model for the standard deviation in the number of counts for a particular pixel at position (i, j) on the camera sensor array:

$$\sigma_{pix}(i,j) = \sqrt{A0 + A1 * N_{pix}(i,j) + A2 * N_{pix}(i,j)^2}, \tag{2}$$

where $N_{pix}(i,j)$ is the mean number of pixel counts at a specific pixel, $A0$ is the read noise term, $A1 * N_{pix}(i,j)$ is the shot noise term, and $A2 * N_{pix}(i,j)^2$ is the intensity noise term.

Around 100 images were captured with the laser incident on the camera sensor using a remote shutter, without adjusting the power output of the laser or adjusting the position of the camera or the laser. Subsequent setups replaced the laser with a green LED in an attempt to mitigate the apparent variation in the position of the beam on the sensor. Once

the images were captured, a Python script was used to find the number of pixel counts at each position in the camera sensor matrix, and then find the mean and standard deviation for the number of pixel counts for each position in the camera sensor matrix. The standard deviation versus the mean number of pixel counts for each position was plotted and fit with the above model in order to determine coefficients of the noise terms, and thus the quantum efficiency of the camera.

3 Results

3.1 Camera Calibration

First, the question of whether the calibration is independent of beam profile was addressed. Results obtained from previous measurements (Figure 5) showed the calibration could be dependent on beam profile [9].

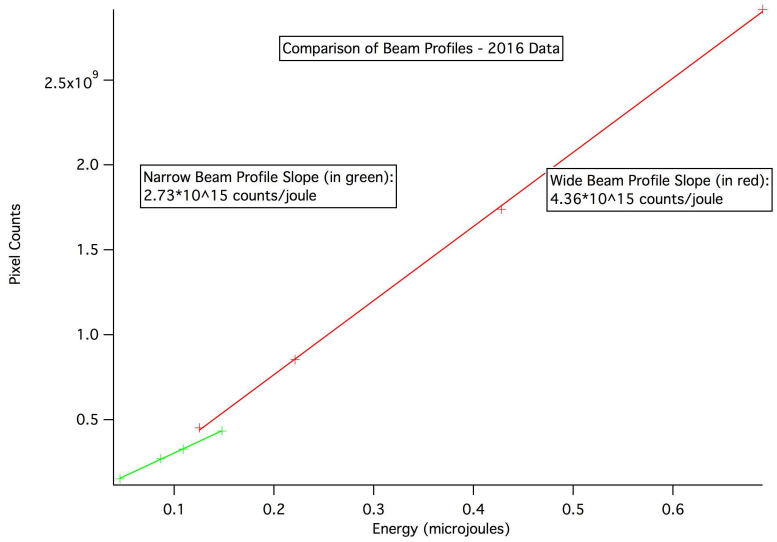

Figure 5: Beam profile calibrations for the green color channel for two different beam profiles from data collected in 2016 by C.J. Xin [9]. Note the significantly different slopes of the two lines.

This result is inconsistent with how the CMOS sensor works. Because the photosensors which make up the CMOS sensor have a linear response between the number of electrons produced and the number of photons incident for a particular wavelength of light, the distribution of light across the sensor should not matter for the digital output (ignoring cases of saturation). This result also poses additional complications for the ultimate experimental goal as the scattering off the test mass will have a different beam profile than the laser used for the calibration.

To address this question, in each set of data a series of exposures were taken with two sets of beam profiles. For every set of data, including those for 1064nm light, the differences between the calibrations of the different beams profiles were found to be small and within the uncertainties of the respective calibration measurements. Further investigation revealed the

previous wide beam results were consistent with the results obtained as part of this project, suggesting that there was an error with the narrow beam measurements from last year.

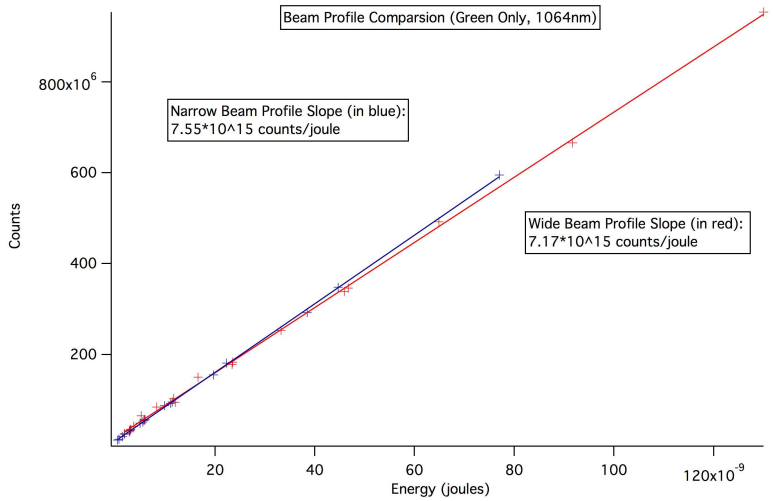

Figure 6: Beam profile calibrations for the green color channel for two different beam profiles. The difference in slopes between the lines is smaller than the 5.12% uncertainty in the slopes of the lines.

After concluding the calibration does not depend on the beam profile of the incident laser, both beam profiles were combined together to find the calibration of the red, green, and blue channels. Energy from ambient light was subtracted from each data point. The measured power incident on the camera sensor was for the whole sensor, not the energy incident on each of the different color channels. Based on the total area each color photosensor occupies in the Bayer array, about 1/4 of the total light is incident on the red and blue sensors, while 1/2 is incident on the green sensors. Table 1 and Table 2, along with the figures in this section, include this adjustment.

Color	Slope (Count/joule)	Uncertainty
Red	$1.66*10^{16}$	5.12%
Green	$1.49*10^{16}$	5.12%
Blue	$1.70*10^{16}$	5.14%

Table 1: Nikon D7100 1064nm Calibration Results at ISO 200.

The calibration was first performed with a Nikon D7100 camera. A second camera, a Nikon D810, was calibrated using an identical procedure.

Color	Slope (Count/joule)	Uncertainty
Red	$7.64*10^{15}$	5.14%
Green	$6.47*10^{15}$	5.15%
Blue	$7.41*10^{15}$	5.16%

Table 2: Nikon D810 1064nm Calibration Results at ISO 200.

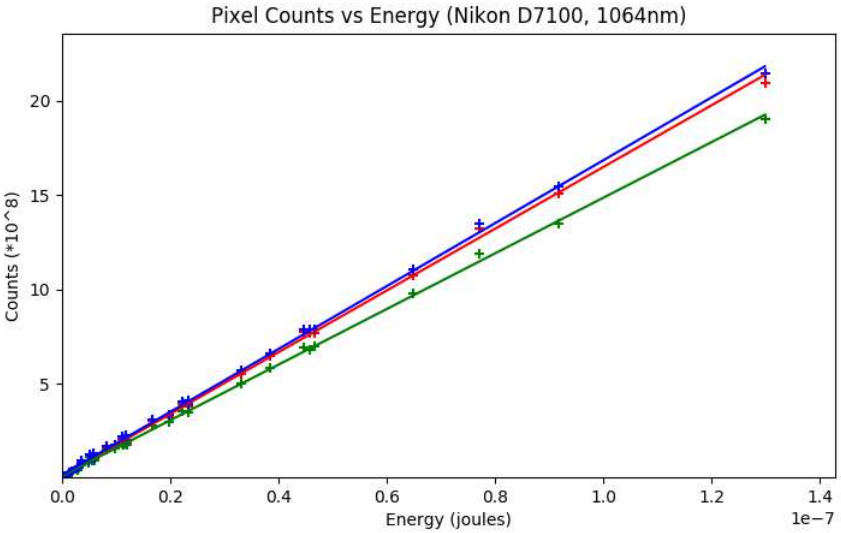

Figure 7: Calibration data for Nikon D7100. Includes red, green, and blue channels.

3.2 Measuring Optical Scattering from LHO Test Masses

A D7100 camera mounted in one of the viewports facing the end test mass in the X-arm (ETMx) used for the photon calibration system was used to measure the amount of power being scattered off the mirror.

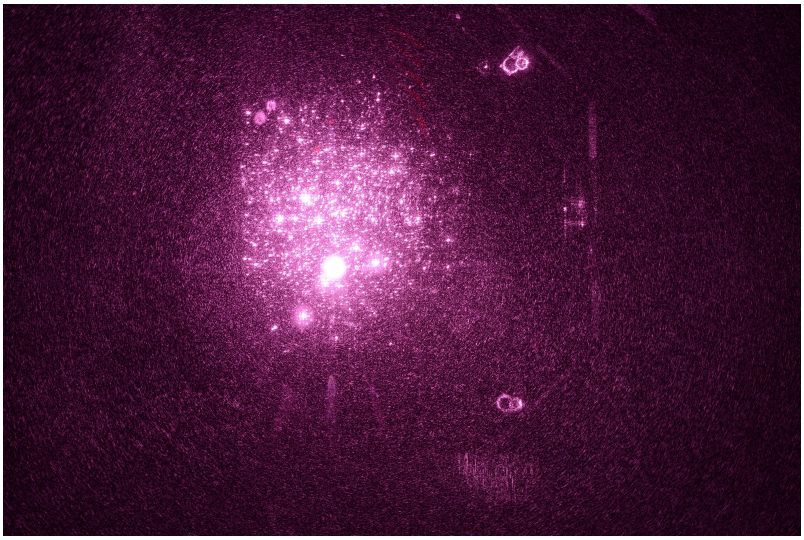

Figure 8: Sample of photo of the ETMx scattering (interferometer locked). Note the saturated pixels, and the red laser light being recorded by the camera as well near the top of the image. The following photo was taken using 1/5 shutter speed and at ISO 100, but even at faster shutter speed, many pixels still saturated.

The pixel counts across the red, green, and blue channels were summed for each image, and the counts were converted into an energy by applying the calibration measured earlier. The amount of power scattered by the mirror was calculated by dividing by the exposure time of the image. Regardless of the exposure time, the power measured by the camera should remain constant.

Read noise (dark noise) was a significant source of noise for exposures taken with quick shutter speeds. Failing to account for the read noise while first analyzing the data resulted in the quick shutter speeds measuring a much larger power than the longer shutter speeds. To get a crude estimate of the read noise of the camera, the lens cap was attached to the DSLR and placed face down on the optical table. Then, exposures were taken across a range of shutter speeds with the lights in the room turned off. This setup prevented the sensor from absorbing photons, and therefore the pixel counts registered by the camera were just from the read noise of the electronics.

A model for the power measured by the camera as a function of the exposure time was developed using this data:

$$log_{10}(P_{rn}) = -log_{10}(t) - 8.83, \tag{3}$$

where P_{rn} is the read noise power and t is the exposure time. At quick shutter speeds (for example, 1/5000 of a second), the read noise power can be about as large or larger than the power incident on the sensor from scattered light. The read noise of the Nikon D7100 (Figure

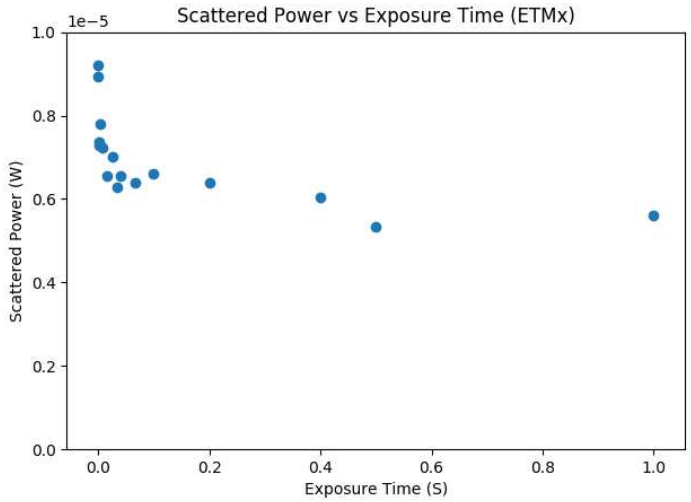

Figure 9: Measured scattered power versus the exposure time for ETMx. The amount of power each photosite measured was calculated then summed together. Multiple exposures with the same shutter speed were averaged together. This figure includes read noise subtraction.

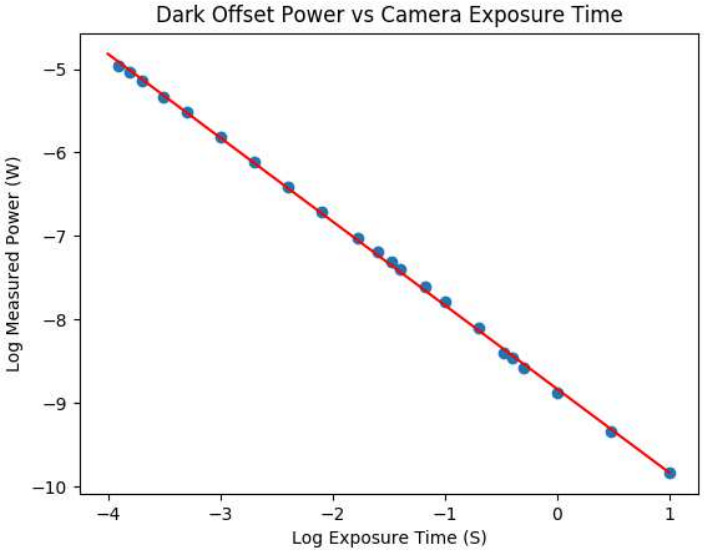

Figure 10: Measurement of the read noise (dark offset) power of the entire sensor. Nikon D7100 at ISO 100.

11) was relatively constant across various shutter speeds. This behavior, along with the read noise of other DSLR cameras used to make these measurements, could be the subject of further investigations. The read noise of the Nikon D810 was much larger than the Nikon D7100 as well, highlighting this as an important feature to characterize when calibrating and measuring power using other cameras. To address the error caused by saturation,

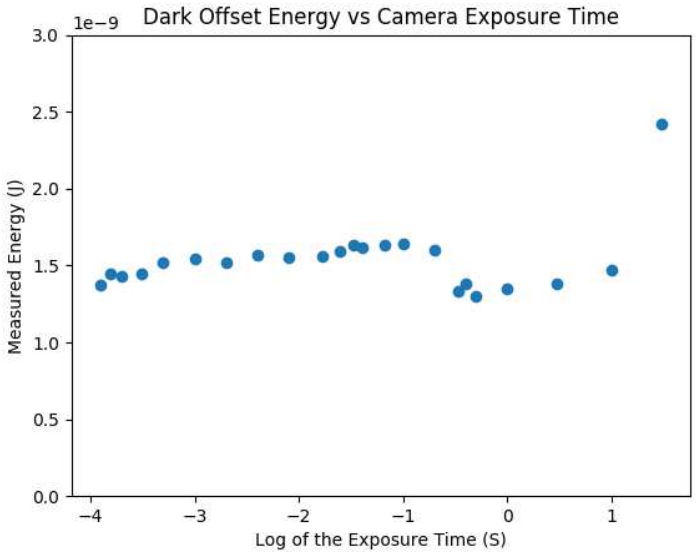

Figure 11: Measurement of the Nikon D7100 read noise energy, summed for the entire sensor. Note the sudden decrease in read noise for images with an exposure speed around one second.

an algorithm was implemented to extend the dynamic range of the camera. Instead of averaging the power measured by the camera from one exposure time, the algorithm used a range of shutter speeds so that saturated pixels were not counted towards the power total, and instead the values for the saturated pixels were obtained from images taken with faster shutter speeds. First, the power from the image with the longest shutter speed was calculated using an identical technique to the method described above. When the script encountered a saturated pixel, its position was recorded, and its power contribution was not counted. After iterating through the entire image, the next slowest exposure time image was analyzed. The algorithm summed the power from the pixels in this image that were not saturated and had not been counted by the previous iterations. This continued until all the pixels had been counted. Read noise power for each shutter speed was subtracted from the total based on the percentage of the total pixels summed for that image. For example, if half of all the pixels in an image were saturated or already counted, the energy contribution from the remaining half would be summed together. The algorithm would therefore subtract only half of the total read noise for that shutter speed using Eq. 3. Extending the dynamic range has a number of benefits. While quick exposure speeds reduce the number of saturated pixels in the image, the read noise of the camera is proportionally much larger. Using longer shutter speeds increases the ratio of the number of counts registered from light to the counts generated by read noise. In order to visualize where most scattered power originated from, Figure 12 was produced using this method of extending the dynamic range.

After estimating the power from the test masses, the distance from the test masses to their respective cameras were found in order to find the radiance of the test mass wide angle scattering. This method is described in a separate paper included in the same DCC entry as this paper [13]. The uncertainty in the camera calibration was the largest source of uncertainty in calculating the radiance, and much larger than the other errors, such as the

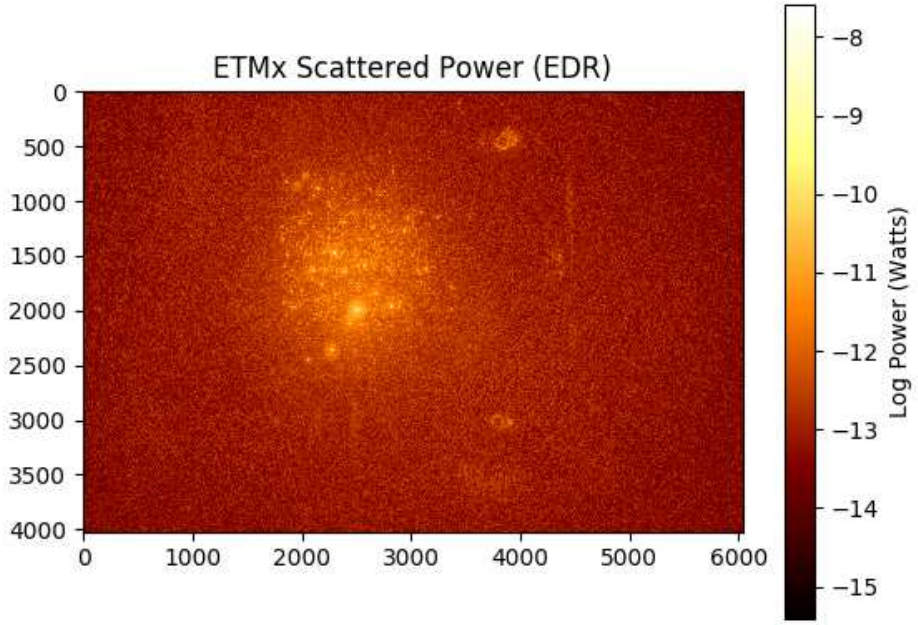

Figure 12: Colormap showing the intensity of the scattered power measured off ETMx. Different positions on the surface scatter orders of magnitude more power than others. Most of the scattering comes from a few very bright spots, rather than being distributed across the surface.

error in distance between the test mass and the camera, the observing area of the camera, and the power measured between different images of the same exposure time. The uncertainty in the power measurement from the PD-300 photodiode (with filter out at 1064nm) [14] was the larger than other sources of uncertainty in the calibration measurement, such as the intensity fluctuations of the laser.

Because the power of the light scattered is dependent on the angle at which it is observed, limited comparisons can be made between the ITMx and ETMx results. The difference in distance between the viewport and the test mass for ITMx and ETMx yields a different angle for observing the scattered light. Measuring scattered light at another angle would be limited to the placement of other viewports. The power circulating in the optical cavities during the two measurements were also different, although the difference would not explain the whole discrepancy between the two results, as the power of the optical cavities, and therefore the power reflected by the test masses, scales linearly with in input power. The transmissivity of the viewports were not accounted for during these calculations.

Test Mass	TM Coor (mm)	Camera Coor (mm)	Camera/TM Distance (mm)	Angle (degrees)
IMTx	(5013, -200, -80)	(32648, 200, 842)	32655	1.52
ETMx	(-502, -200, -80)	(-5652, 566, 509)	5240	10.6

Test Mass	Effective Aperture Area (mm^2)	Measured Power (W)	Uncertainty	Radiance (W/sr)
IMTx	13340	$1.42*10^8$	5%	10.84
ETMx	268	$8.42*10^6$	5%	.0142

Table 3: The radiance and the parameters used in calculating the radiance of ITMx and ETMx.

Another attempt to measure the scattering off the test masses at LHO using photodiodes measured ETMx scattering power to scatter be 2.76 watts/steradian at 7.64° and ITMx to scatter 42.22 watts/steradian at 1.21° [4]. An important note is that in between these measurements, ITMx had been cleaned.

3.3 Camera Sensor Quantum Efficiency

Measuring the quantum efficiency of the camera sensor produced inconclusive results. Plotting the standard deviation versus the mean of pixel counts for each location in the sensor array yields a collection of points with a large spread in their standard deviations, which results in a fit which does not describe the collection of points well (Figure 13).

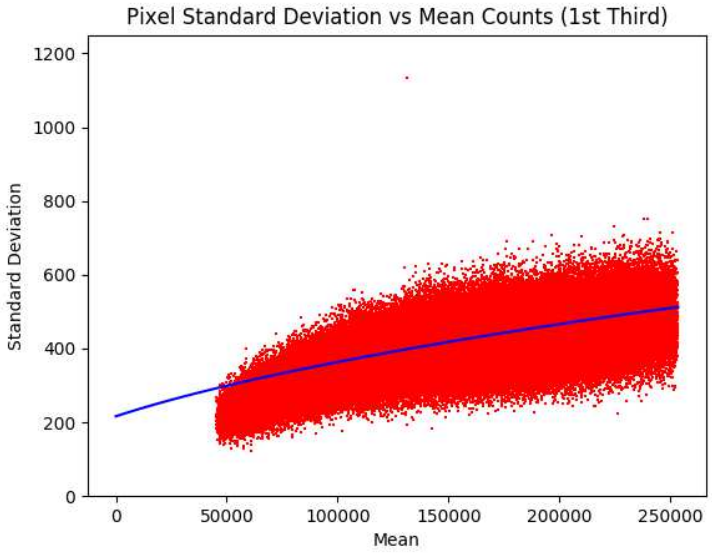

Figure 13: Plot of the standard deviation versus mean pixel counts for a group of 30 exposures illuminated with light from a green LED.

Adding more pictures to the analysis should reduce the spread along the y-axis, as the standard deviation of the mean for one pixel location is inversely proportional to the square root of the number of measurements [15]. However, this did not remedy the situation, and instead introduced much larger variations in the standard deviations in some areas (Figure 14). This was first observed when the light source was a 980nm laser. After comparing images in the data set, the image of the laser was observed to move slightly between exposures, particularly the interference pattern. To remove the the interference fringes, a green LED

was used as the light source instead. While this particular measurement would not be applicable to this project because the quantum efficiency of the sensor is different for green light, it would demonstrate the viability of this measurement technique. However, similar results were observed with the green LED, with the spread in the standard deviation again increasing drastically as images were added.

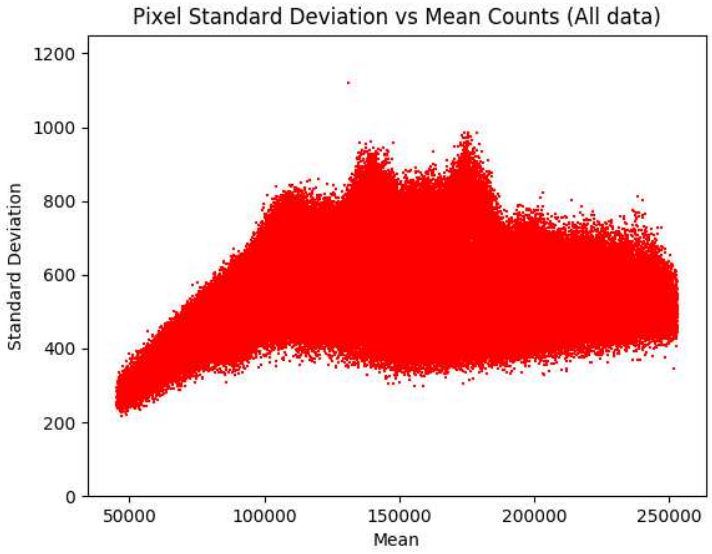

Figure 14: Plot of the standard deviation versus mean pixel counts for a group of 90 exposures illuminated with light from a green LED. The larger variations in the standard deviation appear to come from the position of the LED shifting slightly across the range of images used.

Future work should determine if this effect is indeed caused by the image position shifting and attempt to minimize this effect.

4 Conclusion and Future Work

After calibrating DSLR cameras to measure the energy of light incident on the sensor, images of ETMx and ITMx at LHO were captured in order to measure the wide angle scattering. The camera sensor was further characterized beyond the just calibration in order to obtain a more accurate estimate of the scattering. The radiance of the scattering off ETMx was measured to be 10.42 watts/steradian at an an angle of 10.6°, while ITMx was measured to be .0142 watts/steradian at an angle of 1.52°. Additional work to measure the quantum efficiency of the sensor could yield a more precise result for the amount of power scattered.

O2 was completed near the time when this report was finished. Part of the planned post-O2 commissioning work includes replacing some of the test masses. Characterizing the scattering off the new test masses could be a subject of future investigation. These methods could also be used to monitor the changes in scattering over time, or after commissioning activities such as cleaning the test mass surfaces.

Additional analysis techniques could also be utilized in order to calculate a better estimate for the test mass scattering. Many of the problems encountered in the analysis are similar problems to those found in astronomy and astrophotography, and applying techniques such as stacking as another means to distinguish pixel counts from optical sources as opposed to those from the camera sensor could be utilized. Edge detection software could be utilized in order to examine individual scattering "points" and measure the individual power of each point.

The difference between the measured scattering from ETMx and ITMx is a few orders of manginutude. Additionally, these results are inconsistent with previously reported results [4]. Both of these inconsistencies are not well understood, and warrant further study.

Combining scattering measurements while the interferometer was locked with more detailed characterizations of the wide-angle scattering behavior of the test masses could help resolve the discrepancy between the estimates for the ITMx and ETMx scattering. In order to adequately compare the the two measurements, the angular dependence of the scattering must be answered, work that is difficult to do in the interferometer because of the limited placement of the viewports. With this information, the question whether the ETMx scattering is larger or whether it was observed at an angle which scatters more light could be addressed.

References

[1] LIGO. *LIGO Optics*. URL: `https://www.ligo.caltech.edu/page/optics`.

[2] et al. Elanor King. *Test mass scattering and absorption at LHO*. URL: `https://dcc.ligo.org/LIGO-G1500288`.

[3] Peter R. Saulson. *Fundamentals of Interferometric Gravitational Wave Detectors*. World Scientific, 2015.

[4] Vincent Roma. *Optical Lever and Baffle Diode Information*. URL: `https://dcc.ligo.org/LIGO-T1600085`.

[5] Teledyne Dalsa. *CCD vs CMOS*. URL: https://www.teledynedalsa.com/imaging/knowledge-center/appnotes/ccd-vs-cmos/.

[6] *Digital Camera Sensors*. URL: http://www.cambridgeincolour.com/tutorials/%20camera-sensors.htm.

[7] *Bayer Array Illustration*. URL: http://cdn.cambridgeincolour.com/images/tutorials/sensors_array-color.png.

[8] LIGO. *LIGO Laser*. URL: http://www.ligo.edu/laser.

[9] Chen Jie Xin. *Development of optical imaging system for LIGO test mass contamination and beam position monitoring*. 2016. URL: https://dcc.ligo.org/DocDB/0128/T1600390/002/ligo_final_report.pdf.

[10] *Rawpy*. URL: https://pypi.python.org/pypi/rawpy.

[11] et al. S. Karki. *The Advanced LIGO Photon Calibrators*. 2016. URL: https://arxiv.org/pdf/1608.05055.pdf.

[12] Richard Savage. *ITMX images with newly-installed Pcal-style ITM camera*. URL: https://alog.ligo-wa.caltech.edu/aLOG/index.php?callRep=35327.

[13] Christian Pluchar. *Test Mass Power Scattering Calculations*. URL: https://dcc.ligo.org/LIGO-G1701180.

[14] *PD-300 Photodiode Power Sensor Datasheet*. URL: http://www.ophiropt.com/laser--measurement/sites/default/files/PD300-3W_0.pdf.

[15] John R. Taylor. "An Introduction to Error Analysis". In: University Science Books, 1997.